Shock Compression of Crystalline TeO_2 to the High-Pressure Fluid Regime: Insights from Ab Initio Molecular Dynamics Simulations

Philippe F. Weck[1,*] and Eunja Kim[2]

[1] *Sandia National Laboratories, Albuquerque, New Mexico 87185, USA*
[2] *Department of Physics, The University of Texas at El Paso, El Paso, Texas 79902, USA*

(Dated: August 24, 2024)

The shock response of fully-dense and porous crystalline tellurium dioxide (TeO_2) to the high-pressure and high-temperature fluid regime was investigated within the framework of density functional theory with Mermin's generalization to finite temperatures. The principal and porous shock Hugoniot curves were predicted from canonical *ab initio* molecular dynamics (AIMD) simulations, with the phase space sampled along isotherms up to 80000 K, for densities ranging from $\rho = 3$ to 17 g/cm^3. The polymorphs investigated are $\alpha-TeO_2$ paratellurite ($P4_12_12$), TeO_2 cotunnite ($Pnma$) and TeO_2 post-cotunnite ($P2_1/m$). Based on the discontinuity found in the calculated U_s-u_p slope of TeO_2 post-cotunnite at a shock velocity of $U_s \simeq 8.35$ km/s and a particle velocity of $u_p \simeq 3.64$ km/s, the shock melting temperature and pressure are predicted to be $\simeq 6500$ K and $\simeq 170$ GPa. Results from AIMD simulations are in line with static compression data of TeO_2 paratellurite and cotunnite, and with recent shock Hugoniot data for single-crystal $\alpha-TeO_2$ for pressures to 85 GPa obtained using the inclined-mirror method and velocity interferometer system for any reflector (VISAR) combined with powder gun and two-stage light-gas gun.

PACS numbers:

I. INTRODUCTION

Owing to their outstanding acousto-optic (AO) and electro-optic properties[1–3], crystalline tellurium dioxide (TeO_2) and TeO_2-based glass have attracted considerable attention as technologically important materials in civilian and military fields. Applications for this class of materials range from optical amplifiers to optical switching devices (e.g., optical transistors and ultrafast switching devices), due in particular to their good UV-vis light transmittance and their high linear and nonlinear refractive indices[4,5]. TeO_2 is widely utilized in the production of acousto-optic deflector (AOD), acousto-optic modulator (AOM), acousto-optic tunable filter (AOTF), and active Q-switches and RF spectrum analyzers in laser technology science and optoelectronic technology.

High-performance and high-fidelity of AO devices are typically limited by their structural, thermal and mechanical properties, directly impacting their figure of merit, which is proportional to the AO device diffraction efficiency[6], and their acoustic attenuation, which can cause overheating of the AO device and distortion of optical output[7]. Therefore, understanding the behavior and structure-property relationships of TeO_2 under high-pressure and high-temperature conditions is of paramount importance to assess the reliability of TeO_2-based AO devices subjected to extreme environments.

Two crystalline TeO_2 polymorphs are commonly found around ambient conditions, i.e., the thermodynamically-stable tetragonal $\alpha-TeO_2$ paratellurite phase[8,9] ($P4_12_12$, D_4^4) and the orthorhombic $\beta-TeO_2$ tellurite phase[10,11] ($Pbca$, D_{2h}^{15}). Both phases consist of corner-sharing distorted TeO_4 disphenoids, which are arranged as a fully-connected 3D network in $\alpha-TeO_2$ and a 2D layered network in $\beta-TeO_2$. Early ultrasonic wave propagation and dielectric constant measurements, as well as Raman and Brillouin spectroscopy studies and neutron and X-ray diffraction (XRD) investigations, showed that a pressure-induced phase transition from the tetragonal $\alpha-TeO_2$ phase to the orthorhombic $\gamma-TeO_2$ phase[11] ($P2_12_12_1$, D_2^4), occurs near $\simeq$ 0.9 GPa at room temperature under static compression[12–15]. This second-order phase transition was found to be driven by a soft acoustic mode propagating along the $\langle 110 \rangle$ direction and polarized along the $\langle 1\bar{1}0 \rangle$ direction[13,16]. Similar to the α and β polymorphs, the γ structure is made of corner-sharing distorted TeO_4 disphenoids, although it appears close to a polymeric chain-like structure due to the relative elongation of one of the Te−O bonds within the coordination units[17]. Further compression leads to a first-order phase transition to the orthorhombic cotunnite-structured ($PbCl_2$) TeO_2 polymoprh[18] ($Pnma$, D_{2h}^{16}). A transition pressure of 12 GPa was initially reported for this transformation by Ming and Manghnani[19] using XRD characterization. Subsequent static compression XRD and Raman scattering studies by Liu[20], Jayaraman and Kourouklis[21], and Sato et al.[22] suggested transition pressures of $\simeq$ 25 GPa, $\simeq$ 22−26 GPa, and $\simeq$ 20−30 GPa, respectively. Recent shock compression experiments of $\alpha-TeO_2$ single crystals to 85 GPa by Liu *et al.*[23] using the inclined-mirror method and velocity interferometer system for any reflector (VISAR) combined with powder gun and two-stage light-gas gun indicated a transition pressure of $\simeq 26 \pm 2$ GPa. This finding was confirmed by first-principles calculations at zero temperature predicting this first-order phase transition at 22 GPa[23].

In contrast, relatively few high-pressure studies have focused on cotunnite and post-cotunnite phase transformations in TeO_2. A transformation of TeO_2 cotunnite

to a post-cotunnite phase was first observed by Sato et al.[22] in the pressure range $\simeq$ 80−100 GPa using XRD and Raman scattering techniques with a diamond-anvil cell (DAC). They reported a transformation to a post-cotunnite phase at $\simeq$ 80 GPa after laser heating to above 1000 K, while no indication of a phase transition to a post-cotunnite phase was observed upon room-temperature static compression of TeO_2 to $\simeq$ 100 GPa. Griffiths *et al.*[18] used first-principles AI density functional theory (DFT) methods combined with random-structure searching (AIRSS) to identify possible TeO_2 post-cotunnite structures at 0 K. A transition from cotunnite to a monoclinic TeO_2 post-cotunnite phase[18] ($P2_1/m$, C_{2h}^2) was predicted at $\simeq$ 130 GPa. The AIRSS method also produced a slightly less energetically favorable low-symmetry $P\overline{1}$ structure, along with a couple of low-enthalpy candidate structures crystallizing in the $Cmcm$ and $P2_1/c$ space groups at high pressure.

In this study, the equation of state (EOS) and shock response of fully-dense and porous crystalline TeO_2 to the high-pressure and high-temperature fluid regime is investigated within the framework of DFT with Mermin's generalization to finite temperatures. The principal and porous shock Hugoniot curves are predicted from canonical *ab initio* molecular dynamics (AIMD) simulations, with the phase space sampled along isotherms up to 80,000 K, for densities ranging from ρ = 3 to 17 g/cm^3. The polymorphs investigated are $\alpha-TeO_2$ ($P4_12_12$), TeO_2 cotunnite ($Pnma$) and TeO_2 post-cotunnite ($P2_1/m$). Results from AIMD simulations are compared with the static compression data of TeO_2 paratellurite and cotunnite by Sato et al.[22] and with the recent shock compression experiments of $\alpha-TeO_2$ single crystals by Liu *et al.*[23].

Details of the computational methods utilized in this study are given in Section II, followed by a discussion of our results in Section III. A summary of our findings and conclusion is reported in Section IV.

II. COMPUTATIONAL METHODS

AIMD simulations were conducted using spin-polarized density functional theory with Mermin's generalization to finite temperatures[24], as implemented in the Vienna *ab initio* simulation package (VASP)[25]. The exchange-correlation energy was calculated using the generalized gradient approximation (GGA)[26], with the parameterization of Perdew, Burke, and Ernzerhof (PBE)[27]. Standard functionals such as the PBE and PW91 functionals were found in previous studies to correctly describe experimentally characterized structures and properties of chalcogenide and oxide compounds[28–32]. In particular, recent GGA/PBE calculations demonstrated that this level of theory accurately reproduces the pressure-induced transformation from the orthorhombic $\gamma-TeO_2$ phase to the $PbCl_2$-structured TeO_2 cotunnite phase observed experimentally in the vicinity of $\simeq$ 26 GPa[23]. GGA/PBE was also utilized by Griffiths *et al.* in the first-principles AIRSS search for post-cotunnite structures[18].

The projector augmented wave (PAW) method was utilized to describe the interaction between valence electrons and ionic cores[33,34]. The Te($5s^2, 5p^4$) and O($2s^2, 2p^4$) electrons were treated explicitly as valence states in the Mermin-Kohn-Sham (MKS) equations and PAW pseudopotentials were used to represent the remaining core electrons together with the nuclei. The plane-wave cutoff energy for the electronic wavefunctions was set to 800 eV, ensuring total energy convergence to within 1 meV/atom. Partial occupancies were set for each wavefunction using the Methfessel-Paxton scheme[35].

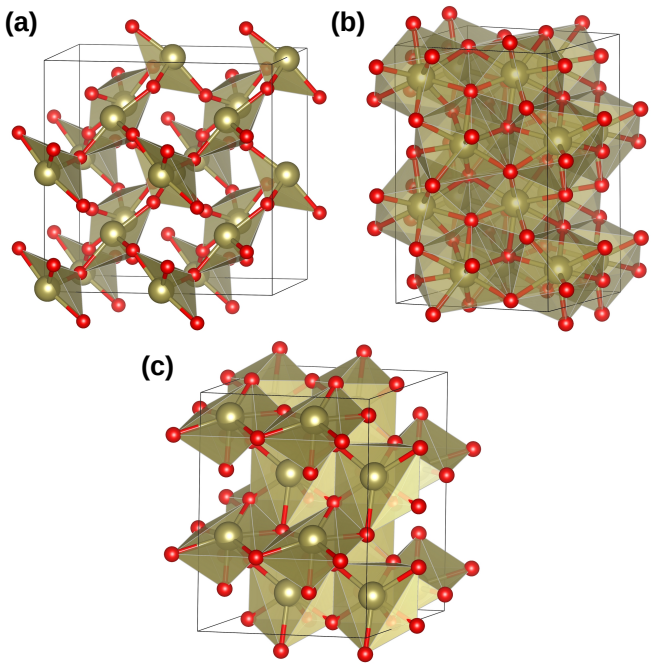

FIG. 1. Periodic crystal supercells of (a) $\alpha-TeO_2$ paratellurite ($2\times2\times1$ supercell, Z = 16; $P4_12_12$, IT No. 92), (b) TeO_2 cotunnite ($2\times2\times1$ supercell, Z = 16; $Pnma$, IT No. 62), and (c) TeO_2 post-cotunnite ($1\times2\times2$ supercell, Z = 16; $P2_1/m$, IT No. 11). Color legend: O, red; Te, gold.

Canonical ensemble (NVT) simulations were conducted using crystal supercells with 3-D periodic boundary conditions applied along isotherms in the range 2000−80000 K for $\alpha-TeO_2$ paratellurite, 300−30000 K for the TeO_2 cotunnite phase, and 1000−30000 K for the TeO_2 post-cotunnite phase. Supercells were built from X-ray diffraction (XRD) data by Thomas[9] for $\alpha-TeO_2$ paratellurite ($2\times2\times1$ supercell, Z = 16; $P4_12_12$, IT No. 92), and by Griffiths *et al.*[18] for TeO_2 cotunnite ($2\times2\times1$ supercell, Z = 16; $Pnma$, IT No. 62) and TeO_2 post-cotunnite ($1\times2\times2$ supercell, Z = 16; $P2_1/m$, IT No. 11). Supercells were utilized in the simulations to ensure that

the interaction of molecular structures with their periodic images is negligible. Crystal supercells of the $\alpha-$, cotunnite and post-cotunnite TeO_2 structures are displayed in Figure 1. Densities in the ranges 3−17 g/cm^3 for $\alpha-TeO_2$, 4−13 g/cm^3 for cotunnite, and 4−12.5 g/cm^3 for post-cotunnite, in increments of 0.5 or 1.0 g/cm^3, were used in AIMD simulations. Previous computational studies of EOS and shock properties showed that such grid spacings provide a good balance between error introduced by bi-rational interpolation and AIMD computational time to generate each (P,T) point. Baldereschi's mean-value special k-point[36] was utilized for properties averaging in the Brillouin zone. A time step of 0.7 fs for ion-motion was set, with velocities scaled at each simulation step to the temperature, and each NVT simulation was run for up to $\simeq 10-15$ ps. Equilibration was achieved when the block average[37] of the standard deviation of the pressure was less than $\simeq 0.5\%$.

The principal shock Hugoniot was predicted from the tabular EOS obtained from the present AIMD simulations, using as a reference state the fully-dense $\alpha-TeO_2$ bulk paratellurite ($\rho_0 = 6.024$ g/cm^3) characterized experimentally under ambient temperature and pressure conditions[9]. The shock Hugoniot curve consists of the locus of all (P,V,T) points which satisfy the Rankine-Hugoniot relation,

$$E - E_0 + (1/2)(P + P_0)(V - V_0) = 0, \qquad (1)$$

where E is the specific internal energy, P is the pressure, $V = 1/\rho$ is the specific volume of the shocked bulk structure, and E_0 and P_0 are the reference energy and pressure obtained from AIMD simulation of fully-dense bulk paratellurite at 300 K. The Hugoniot points were calculated through a series of NVT simulations at multiple temperatures, for successive isotropically-compressed specific volumes from ambient to elevated pressure. For each specific volume, the Hugoniot state was obtained by interpolating the two (P,T) points which bracket the Hugoniot temperature and pressure. To find the Hugoniot locus of shock states, we solved Eq. (1) for each density/temperature pair along an isotherm. We then interpolated between the two densities that bounded where the Rankine-Hugoniot conditions are satisfied to find the density, pressure, and energy of the Hugoniot for that temperature. To solve the Rankine-Hugoniot relation for initially porous TeO_2, the full-density volume V_0 was replaced with the initial porous volume $V_{00} = 1/\rho_{00}$ in Eq. (1), while the reference energy E_0 and pressure P_0 of the full-density bulk paratellurite at ambient conditions were conserved. This computational method to predict the principal and porous Hugoniot was successfully validated in previous studies by direct comparison of computational results derived from tabular EOS with shock data for several metals and oxides[29–32,38].

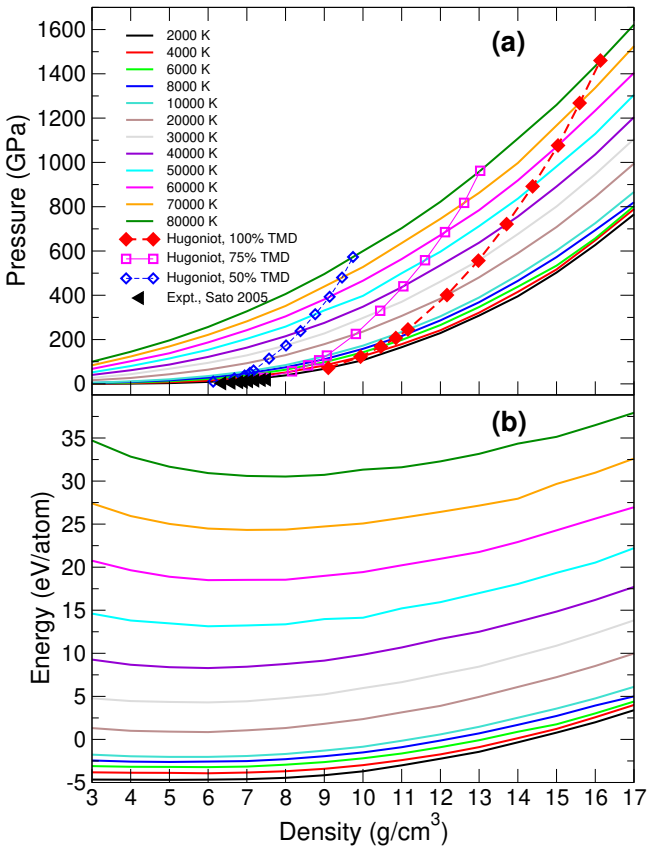

FIG. 2. (a) Pressure and (b) specific internal energy of $\alpha-TeO_2$ paratellurite ($2\times2\times1$ supercell, $Z = 16$; $P4_12_12$, IT No. 92) as a function of density calculated from AIMD/PBE simulations along isotherms between 2000 and 80000 K. The computed principal Hugoniot and porous Hugoniot for initial densities of 50 and 75% of the theoretical maximum density (TMD; $\rho_0 = 6.024$ g/cm^3 at 300 K) are shown in (a), along with the static compression DAC data of $\alpha-TeO_2$ paratellurite for samples preheated to above 1000 K before the shock by Sato *et al.* [22].

III. RESULTS AND DISCUSSION

Figure 2 displays the variation of the pressure and specific internal energy of the $\alpha-TeO_2$ paratellurite $2 \times 2 \times 1$ supercell as a function of density calculated from AIMD/PBE simulations along isotherms between 2000 and 80000 K. The computed principal Hugoniot and porous Hugoniot for initial densities of 50 and 75% of the theoretical maximum density (TMD; $\rho_0 = 6.024$ g/cm^3) are also shown. The reference energy and pressure obtained from AIMD simulations at 300 K for the full-density $\alpha-TeO_2$ reference structure are $E_0 = -5.288$ eV/atom and $P_0 = 3.23$ GPa. Using these values in Eq. (1), the principal and porous Hugoniot curves were computed by interpolating, for each specific volume, (P,T) points which bracket the Hugoniot tem-

perature and pressure.

TABLE I. Principal and porous Hugoniot states for $\alpha-TeO_2$ paratellurite ($P4_12_12$), with initial solid densities of 100, 75 and 50% of the theoretical maximum density (TMD; ρ_0 = 6.024 g/cm^3 at 300 K), calculated from canonical AIMD/PBE simulations.

ρ_0 (g/cm^3)	T (K)	ρ (g/cm^3)	P (GPa)	u_p (km/s)	U_s (km/s)
6.024	2000	9.104	72.0	1.96	5.81
(100% TMD)	4000	9.937	122.5	2.79	7.09
	6000	10.463	168.2	3.40	8.03
	8000	10.849	207.0	3.87	8.72
	10000	11.162	245.5	4.30	9.34
	20000	12.169	401.0	5.77	11.43
	30000	12.981	556.3	7.01	13.08
	40000	13.709	721.2	8.17	14.58
	50000	14.381	891.8	9.25	15.93
	60000	15.037	1076.3	10.33	17.23
	70000	15.595	1268.0	11.35	18.49
	80000	16.134	1460.0	12.31	19.64
4.518	2000	7.418	27.0	0.86	4.58
(75% TMD)	4000	8.165	56.6	1.52	5.81
	6000	8.582	83.5	1.99	6.68
	8000	8.868	106.4	2.34	7.30
	10000	9.067	127.8	2.63	7.85
	20000	9.816	225.4	3.77	9.77
	30000	10.444	329.9	4.79	11.31
	40000	11.042	440.5	5.74	12.63
	50000	11.603	558.2	6.65	13.84
	60000	12.119	685.0	7.54	15.00
	70000	12.612	817.2	8.40	16.08
	80000	13.028	962.0	9.25	17.20
3.012	2000	6.130	10.1	0.14	8.10
(50% TMD)	4000	6.676	24.6	0.58	6.03
	6000	6.943	37.8	0.87	6.58
	8000	7.080	49.7	1.07	7.19
	10000	7.174	60.6	1.23	7.71
	20000	7.573	114.1	1.94	9.48
	30000	8.011	173.4	2.64	10.67
	40000	8.386	238.3	3.31	11.77
	50000	8.765	314.5	4.02	12.85
	60000	9.139	393.1	4.69	13.77
	70000	9.458	479.9	5.36	14.76
	80000	9.742	572.9	6.00	15.74

The calculated principal and porous Hugoniot states for $\alpha-TeO_2$ paratellurite are summarized in Table I. The particle velocity, u_p, and shock velocity, U_s, were also computed from the AIMD-generated tabular EOS. Based on the conservation equations, these velocities can be expressed as

$$u_p = \sqrt{\frac{P-P_0}{\rho_0}}\sqrt{1-\frac{\rho_0}{\rho}} \quad (2)$$

and

$$U_s = \sqrt{\frac{P-P_0}{\rho_0}}/\sqrt{1-\frac{\rho_0}{\rho}}. \quad (3)$$

As represented in Figure 2 (a), AIMD results for the low-pressure portion of the 2000 K isotherm are in close agreement with the static compression DAC data of $\alpha-TeO_2$ paratellurite for samples preheated to above 1000 K reported by Sato *et al.*[22]. Sato *et al.*[22] indicated that paratellurite does not show any indication of a major phase transformation up to $\simeq$ 20 GPa, consistent with previous experimental findings by Liu[20] and Jayaraman and Kourouklis[21].

To investigate the impact of porosity on shock response, porous Hugoniot curves for samples with 75 and 50% TMD of $\alpha-TeO_2$ paratellurite were calculated from the AIMD-generated tabular EOS. As shown in Figure 2 (a), porous Hugoniot curves do not depart significantly from the principal Hugoniot at very lower pressure and temperature, although noticeable differences are observed at higher $P-T$ conditions, with higher temperatures reached at lower pressure for porous Hugoniot curves compared to the principal Hugoniot (see Table I).

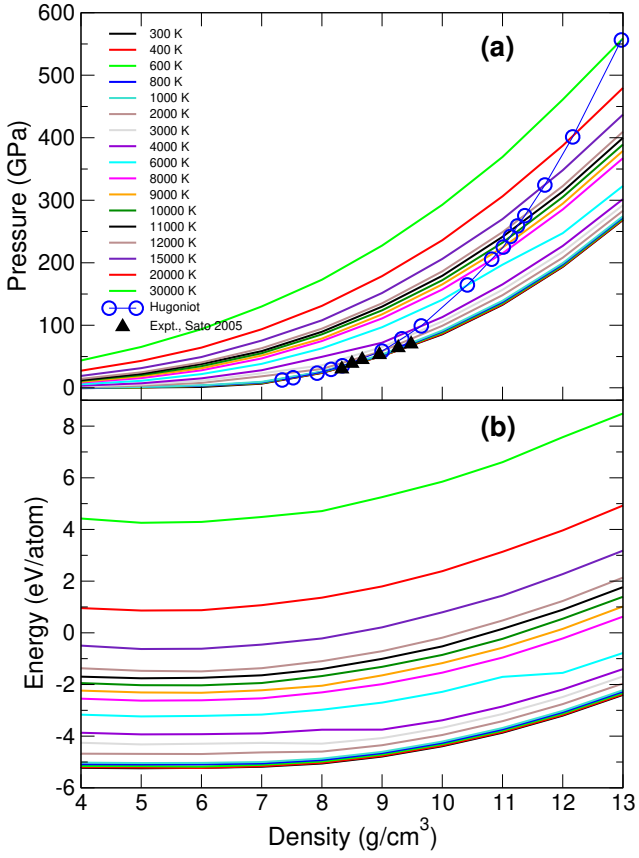

FIG. 3. (a) Pressure and (b) specific internal energy of TeO_2 cotunnite ($2\times2\times1$ supercell, $Z = 16$; $Pnma$, IT No. 62) as a function of density calculated from AIMD/PBE simulations along isotherms between 300 and 30000 K. The computed principal Hugoniot is also displayed in (a), along with the static compression DAC data of TeO_2 cotunnite for samples preheated to above 1000 K before the shock by Sato *et al.* [22].

TABLE II. Principal Hugoniot states for TeO_2 cotunnite ($Pnma$) calculated from canonical AIMD/PBE simulations along isotherms between 300 and 30,000 K. Fully-dense $\alpha-TeO_2$ bulk paratellurite at 300 K (ρ_0 = 6.024 g/cm^3) is utilized as a reference state in Hugoniot calculations.

T (K)	ρ (g/cm^3)	P (GPa)	u_p (km/s)	U_s (km/s)
300	7.341	12.4	0.52	2.92
400	7.526	16.1	0.65	3.27
600	7.911	23.3	0.89	3.74
800	8.148	29.4	1.06	4.08
1000	8.335	35.0	1.20	4.36
2000	8.995	58.6	1.74	5.27
3000	9.316	78.0	2.09	5.92
4000	9.647	98.5	2.43	6.49
6000	10.401	163.3	3.34	7.94
8000	10.808	203.9	3.84	8.67
9000	10.996	224.0	4.07	9.00
10000	11.127	241.3	4.25	9.28
11000	11.258	260.2	4.45	9.57
12000	11.368	276.1	4.61	9.81
15000	11.700	324.6	5.08	10.48
20000	12.169	403.0	5.78	11.46
30000	12.980	556.9	7.01	13.09

The evolution of the pressure and specific internal energy of the TeO_2 cotunnite $2\times2\times1$ supercell with density, predicted from AIMD/PBE simulations in the temperature range 300−30000 K, is depicted in Figure 3. The principal Hugoniot states for TeO_2 cotunnite, computed using the TMD of bulk paratellurite at 300 K as a reference, are also shown in Figure 3 (a) and given in Table II. The $P-\rho$ compression results along the 300−1000 K isotherms reproduce well the static compression DAC data of TeO_2 cotunnite for samples preheated to above 1000 K obtained by Sato *et al.*[22], in the pressure range 30−70 GPa. The calculated Hugoniot appears slightly stiffer along the 3000 and 4000 K isotherms compared to the DAC data. A discontinuity is found along the 4000 K isotherm, corresponding to a pressure of $\simeq$ 73 GPa at a density of $\simeq$ 9 g/cm^3, and shifts to a higher pressure of $\simeq$ 195 GPa and density of $\simeq$ 11 g/cm^3 along the 6000 K isotherm. A similar discontinuity is also reflected in the principal Hugoniot between shock states at 4000 K and 6000 K. This could tentatively stem from the melt transition of the TeO_2 cotunnite phase.

Figure 4 shows the variation of the pressure and specific internal energy of the TeO_2 post-cotunnite $1\times2\times2$ supercell as a function of density, as predicted from AIMD/PBE simulations in the temperature range 1000−30000 K. Predictions of the principal Hugoniot states for TeO_2 post-cotunnite using the TMD of bulk paratellurite at 300 K as a reference are depicted in Figure 4 (a) and summarized in Table III. Similar to cotunnite, as shown in Figures 4 (a) and (b), a noticeable discontinuity appears in the 2000 to 5000 K isotherms, which corresponds to melting of TeO_2 post-cotunnite. This melt transition discontinuity shifts gradually to higher densities at higher P-T, with coarse estimates of

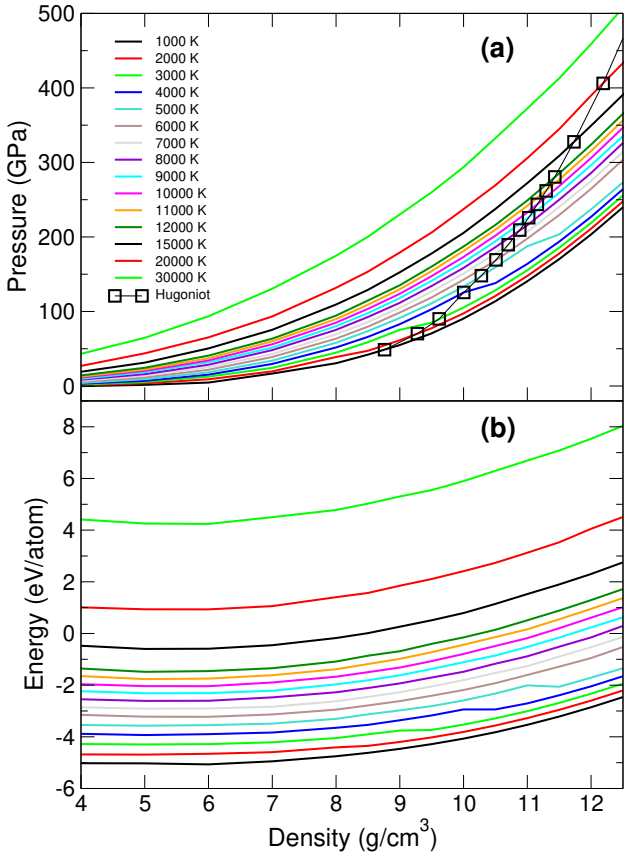

FIG. 4. (a) Pressure and (b) specific internal energy of TeO_2 post-cotunnite ($1\times2\times2$ supercell, Z = 16; $P2_1/m$, IT No. 11) as a function of density calculated from AIMD/PBE simulations along isotherms between 1000 and 30000 K. The computed principal Hugoniot is also displayed in (a).

the pressure, density and temperature (P_m; ρ_m; T_m) corresponding to the melting points under pressure at (38 GPa; 8 g/cm^3; 2000 K), (74 GPa; 9 g/cm^3; 3000 K), (127 GPa; 10 g/cm^3; 4000 K) and (184 GPa; 11 g/cm^3; 5000 K). It is worth noting that AIMD melting simulations would typically require much larger simulations supercells and longer simulation time to accurately determine the melt transition. Under ambient pressure, the measured melting point of TeO_2 is $\simeq$ 1006 K ($\sim$ 733°C).

To determine more accurately the shock melting temperature and pressure of TeO_2 post-cotunnite, the principal Hugoniot predicted from AIMD simulations was converted to the U_s-u_p representation and linear fits to the solid and liquid portions of the Hugoniot were calculated (see Figure 5). The linear fits to the post-cotunnite and liquid portions of the principal Hugoniot are $U_s = 2.417 + 1.631u_p$ and $U_s = 3.003 + 1.470u_p$, respectively. The intersection of both linear fits corresponds to $U_s \simeq 8.35$ km/s and $u_p \simeq 3.64$ km/s, which in turn translates into shock melting temperature and pressure of $\simeq$ 6500 K and $\simeq$ 170 GPa. These values are in

TABLE III. Principal Hugoniot states for TeO_2 post-cotunnite ($P2_1/m$) calculated from canonical AIMD/PBE simulations along isotherms between 1000 and 30000 K. Fully-dense $\alpha-TeO_2$ bulk paratellurite ($\rho_0 = 6.024$ g/cm^3) is utilized as a reference state in Hugoniot calculations.

T (K)	ρ (g/cm^3)	P (GPa)	u_p (km/s)	U_s (km/s)
1000	8.749	48.5	1.53	4.91
2000	9.275	70.3	1.97	5.63
3000	9.626	90.0	2.32	6.20
4000	10.001	125.5	2.84	7.14
5000	10.247	146.1	3.12	7.58
6000	10.517	169.2	3.43	8.03
7000	10.701	189.5	3.67	8.41
8000	10.877	208.5	3.89	8.73
9000	11.022	226.6	4.10	9.04
10000	11.165	244.5	4.29	9.32
11000	11.287	261.9	4.47	9.59
12000	11.412	278.9	4.64	9.84
15000	11.725	327.1	5.11	10.51
20000	12.196	406.9	5.82	11.50
30000	12.500	506.8	6.58	12.70

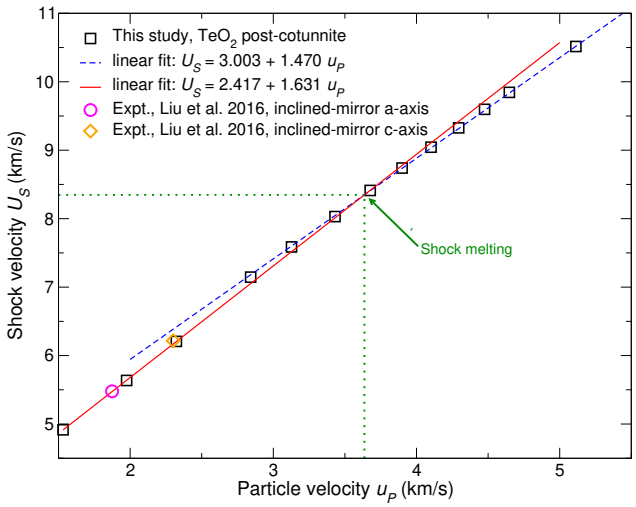

FIG. 5. Shock velocity, U_s, as a function of the particle velocity, u_p, for TeO_2 post-cotunnite ($1 \times 2 \times 2$ supercell, $Z = 16$; $P2_1/m$, IT No. 11) calculated from AIMD/PBE simulations. Linear fits to the solid and liquid portions of the Hugoniot predicted from AIMD simulations are provided to identify the shock melting temperature and pressure based on the discontinuity in the U_s-u_p slope at $U_s \simeq 8.35$ km/s and $u_p \simeq 3.64$ km/s. These values correspond to shock melting temperature and pressure of $\simeq 6500$ K and $\simeq 170$ GPa. Experimental shock Hugoniot data for single-crystal TeO_2 obtained by Liu *et al.* [23] using the inclined-mirror method are shown for comparison.

the ballpark of typical values for shock melting of dioxides. For example, recent experimental and computational investigation of TiO_2 found linear fits intersecting at $U_s \simeq 10.4$ km/s and $u_p \simeq 3.8$ km/s, which corresponds to a pressure of 170 GPa[30]. In SiO_2 and in its dense SiO_2 stishovite form, melting was observed at 5000 K and 8300 K, respectively[39,40]. Let us note also that the experimental shock Hugoniot data for single-crystal TeO_2 obtained by Liu *et al.*[23] at $U_s = 5.478$ km/s and $u_p = 1.874$ km/s (a-axis) and $U_s = 6.217$ km/s and $u_p = 2.301$ km/s (c-axis) using the inclined-mirror method are accurately reproduced by AIMD simulations of TeO_2 post-cotunnite and consistent with the proposed linear fit of solid TeO_2 in the vicinity of the melt transition (see Figure 5).

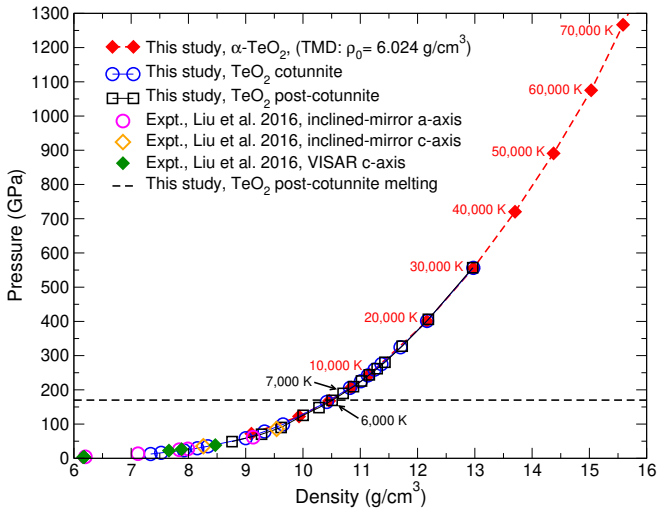

FIG. 6. Pressure-density relationship along the principal Hugoniot of bulk TeO_2 calculated from the AIMD/PBE-generated tables. Principal Hugoniot curves computed using $\alpha-TeO_2$ paratellurite, TeO_2 cotunnite, and TeO_2 post-cotunnite supercells are represented. Experimental shock Hugoniot data for single-crystal TeO_2 for pressures to 85 GPa obtained by Liu *et al.* [23] using the inclined-mirror method and velocity interferometer system for any reflector (VISAR) combined with powder gun and two-stage gas gun are also displayed. The shock melting pressure of TeO_2 post-cotunnite at $\simeq 170$ GPa predicted from AIMD simulations is indicated by a horizontal dashed line.

Finally, the principal Hugoniot curves of TeO_2 computed to 70000 K using the AIMD tabular EOS of this study for paratellurite, cotunnite, and post-cotunnite supercells are shown in the $P-\rho$ representation and compared with the experimental shock Hugoniot data for single-crystal TeO_2 for pressures to 85 GPa obtained by Liu *et al.*[23] using the velocity interferometer system for any reflector (VISAR) and inclined-mirror method and combined with powder gun and two-stage gas gun (Figure 6). Good overall agreement is achieved between principal Hugoniot states predicted from AIMD simulations and VISAR and inclined-mirror method shock data. As expected, in the liquid regime above the shock melting pressure of $\simeq 170$ GPa limited differences exist between calculated paratellurite, cotunnite and post-cotunnite Hugoniot states. A series of magnetically accelerated flyer-

plate shock compression experiments using Z machine at Sandia National Laboratories is planned to validate the present AIMD predictions for the principal Hugoniot of bulk TeO_2.

IV. CONCLUSION

In summary, the EOS of TeO_2 was investigated using canonical AIMD simulations for the paratellurite ($P4_12_12$), cotunnite ($Pnma$) and post-cotunnite ($P2_1/m$) polymorphs and their shock compression response to the high-pressure and high-temperature fluid regime was predicted based on the tabular EOS developed in this study.

AIMD results are in close agreement with the static compression DAC data of paratellurite and cotunnite samples preheated to above 1000 K reported by Sato and coworkers. For cotunnite, a discontinuity in both $P-\rho$ and $E-\rho$ representations is found along the 4000 K isotherm, corresponding to a pressure of $\simeq 73$ GPa at a density of $\simeq 9$ g/cm^3, and shifts to a higher pressure of $\simeq 195$ GPa and density of $\simeq 11$ g/cm^3 along the 6000 K isotherm. This discontinuity is also reflected in the principal Hugoniot between shock states at 4000 K and 6000 K, and can be tentatively be ascribed to the melt transition of the TeO_2 cotunnite phase. Similar to cotunnite, a noticeable discontinuity corresponding to the melt transition of post-cotunnite appears along the 2000 K to 5000 K isotherms for. This melt transition discontinuity shifts gradually to higher densities at higher P-T, with coarse estimates of the pressure, density and temperature $(P_m; \rho_m; T_m)$ corresponding to the melting points under pressure at (38 GPa; 8 g/cm^3; 2000 K), (74 GPa; 9 g/cm^3; 3000 K), (127 GPa; 10 g/cm^3; 4000 K) and (184 GPa; 11 g/cm^3; 5000 K). Based on the discontinuity found in the calculated U_s-u_p slope of TeO_2 post-cotunnite at a shock velocity of $U_s \simeq 8.35$ km/s and a particle velocity of $u_p \simeq 3.64$ km/s, the shock melting temperature and pressure are predicted to be $\simeq 6500$ K and $\simeq 170$ GPa. Results from AIMD simulations are also in line with recent shock Hugoniot data for single-crystal paratellurite obtained by Liu and coworkers using the VISAR and inclined-mirror methods combined with powder gun and two-stage light-gas gun.

Magnetically accelerated flyer-plate shock compression experiments using Z machine at Sandia National Laboratories are planned to validate the present AIMD predictions for the principal Hugoniot of bulk TeO_2 and an extensive comparison of the new shock data with the present AIMD predictions will be reported in due course.

Acknowledgment

Sandia National Laboratories is a multi-mission laboratory managed and operated by National Technology & Engineering Solutions of Sandia, LLC (NTESS), a wholly owned subsidiary of Honeywell International Inc., for the U.S. Department of Energy's National Nuclear Security Administration (DOE/NNSA) under contract DE-NA0003525. This written work is authored by an employee of NTESS. The employee, not NTESS, owns the right, title and interest in and to the written work and is responsible for its contents. Any subjective views or opinions that might be expressed in the written work do not necessarily represent the views of the U.S. Government. The publisher acknowledges that the U.S. Government retains a non-exclusive, paid-up, irrevocable, world-wide license to publish or reproduce the published form of this written work or allow others to do so, for U.S. Government purposes. The DOE will provide public access to results of federally sponsored research in accordance with the DOE Public Access Plan.

* Email: pfweck@sandia.gov

[1] G. Arlt and H. Schweppe, Solid State Commun. **6**, 783 (1968).
[2] Y. Ohmachi and N. Uchida, J. Appl. Phys. **41**, 2307 (1970).
[3] A. Jha, B. D. O. Richards, G. Jose, T. Toney Fernandez, C. J. Hill, J. Lousteau, and P. Joshi, International Materials Reviews **57**, 357 (2012).
[4] A. K. Yakhkind, J. Am. Ceram. Soc. **49**, 670 (1966).
[5] H. Takebe, S. Fujino, and K. Morinaga, J. Am. Ceram. Soc. **77**, 2455 (1994).
[6] I. Chang, Opt. Eng. **24**, 132 (1985).
[7] T. Woodruff and H. Ehrenreich, Phy. Rev. **123**, 1553 (1961).
[8] D. M. Korn, A. S. Pine, G. Dresselhaus, and T. B. Reed, Phy. Rev. B **8**, 768 (1973).
[9] P. A. Thomas, J. Phys. C: Solid State Phys. **21**, 4611 (1988).
[10] H. Beyer, Z. Kristallogr. **124**, 228 (1967).
[11] J. C. Champarnaud-Mesjard, S. Blanchandin, P. Thomas, A. Mirgorodsky, T. Merle-Mejean, and B. Frit, J. Phys. Chem. Solids **61**, 1499 (2000).
[12] P. S. Peercy and I. J. Fritz, Phys. Rev. Lett. **32**, 466 (1974).
[13] P. S. Peercy, I. J. Fritz, and G. A. Samara, J. Phys. Chem. Solids **36**, 1105 (1975).
[14] T. G. Worlton and R. A. Beyerlein, Phys. Rev. B **12**, 1899 (1975).
[15] E. F. Skelton, J. L. Feldman, C. Y. Liu, and I. L. Spain, Phy. Rev. B **13**, 2605 (1976).
[16] M. Ahart, T. Yagi, and Y. Takagi, Jpn. J. Appl. Phys. **35**, 2882 (1996).
[17] Y. Li, W. Fan, H. Sun, X. Cheng, P. Li, and X. Zhao, J. Appl. Phys. **107**, 093506 (2010).
[18] G. I. G. Griffiths, R. J. Needs, and C. J. Pickard, Phys. Rev. B **80**, 184115 (2009).
[19] L. C. Ming and M. H. Manghnani, *High-Pressure Research in Geophysics*, edited by S. Akimoto and M. H. Manghnani (Tokyo: Center Academic Publications Japan, 1982) p.

329.
[20] L. Liu, J. Phys. Chem. Solids **48**, 719 (1987).
[21] A. Jayaraman and G. A. Kourouklis, Pramana-J. Phys. **36**, 133 (1991).
[22] T. Sato, N. Funamori, T. Yagi, and N. Miyajima, Phy. Rev. B **72**, 092101 (2005).
[23] X. Liu, T. Mashimo, N. Kawai, T. Sekine, Z. Zeng, and X. Zhou, Mater. Res. Express **3**, 076206 (2016).
[24] N. D. Mermin, Phys. Rev. **137**, A1441 (1965).
[25] G. Kresse and J. Furthmüller, Phys. Rev. B **54**, 11169 (1996).
[26] J. P. Perdew, J. A. Chevary, S. H. Vosko, K. A. Jackson, M. R. Pederson, D. J. Singh, and C. Fiolhais, Phys. Rev. B **46**, 6671 (1992).
[27] J. P. Perdew, K. Burke, and M. Ernzerhof, Phys. Rev. Lett. **77**, 3865 (1996).
[28] P. F. Weck, E. Kim, and K. R. Czerwinski, Dalton Trans. **42**, 15288 (2013).
[29] P. F. Weck, K. R. Cochrane, S. Root, J. M. D. Lane, L. Shulenburger, J. H. Carpenter, T. Sjostrom, T. R. Mattsson, and T. J. Vogler, Phys. Rev. B **97**, 125106 (2018).
[30] S. Duwal, C. A. McCoy, P. F. Weck, P. Kalita, H. L. Hanshaw, K. R. Cochrane, T. Ao, and S. Root, Phys. Rev. B **102**, 024105 (2020).
[31] P. F. Weck, K. R. Cochrane, and N. W. Moore, AIP Conference Proceedings **2272**, 070053 (2020).
[32] P. F. Weck and N. W. Moore, Chem. Phys. Lett. **831**, 140851 (2023).
[33] P. E. Blöchl, Phys. Rev. B **50**, 17953 (1994).
[34] G. Kresse and D. Joubert, Phys. Rev. B **59**, 1758 (1999).
[35] M. Methfessel and A. T. Paxton, Phys. Rev. B **40**, 3616 (1989).
[36] A. Baldereschi, Phys. Rev. B **7**, 5212 (1973).
[37] M. P. Allen and D. J. Tildesley, *Computer Simulations of Liquids* (Oxford Science Publications, 1987).
[38] E. Kim, P. F. Weck, and T. R. Mattsson, Journal of Applied Physics **124**, 035903 (2018).
[39] D. G. Hicks, T. R. Boehly, J. H. Eggert, J. E. Miller, P. M. Celliers, and G. Collins, Phys. Rev. Lett. **97**, 025502 (2006).
[40] M. Millot, Phys. Plasmas **23**, 014503 (2016).